Experimental Investigation of Wire Arc Additive Manufacturing of Inconel 625 Using Spot Welding

Vojtěch Votruba (V.Votruba@rcmt.cvut.cz)
Czech Technical University in Prague https://orcid.org/0000-0001-6216-4471
Ivan Diviš
Lucie Pilsová
Pavel Zeman
Libor Beránek
Jakub Horváth
Jan Smolík

Research Article

Keywords: Wire Arc Additive Manufacturing, Cold metal transfer, Welding strategy, Inconel 625, Material properties

Posted Date: April 18th, 2022

DOI: https://doi.org/10.21203/rs.3.rs-1525040/v1

Abstract

Additive manufacturing (AM) is a progressive technology which holds promise for manufacturing of heat resistant super alloys. One of the most productive methods is Wire Arc Additive Manufacturing (WAAM). In this article an alternative WAAM welding strategy is investigated. Experimental welds and material tests were performed to evaluate the material properties obtained through a GMAW CMT spot welding strategy used in WAAM of Inconel 625 alloy. The GMAW CMT spot welding strategy has lower productivity and a higher consumption of shielding gas. However, it excels in low heat input and precise material cladding in comparison with a standard GMAW CMT continuous welding strategy. It enables fabrication of finer details even on thin walled components or in sections with problematic heat dissipation. Samples manufactured using this strategy were also compared with samples manufactured through a standard GMAW CMT continuous welding strategy. Two sets of manufactured samples were thus tested. The following material tests were performed: i) metallographic analysis, ii) x-ray tomography, iii) SEM analysis, iv) hardness, v) tensile strength (20°C, 650°C), and vi) pin-on-disc (20°C, 650°C). The results show that the spot welding strategy led to improved material properties in the Inconel 625 samples. Ultimate tensile strength improved by 15% at 20°C and by 4% at 650°C. Wear resistance at 650°C was about two times higher. This paper concludes that the GMAW CMT spot welding strategy for Inconel 625 is definitely suitable for WAAM manufacturing of complex shapes, fine details and thin walled components.

1 Introduction

Heat resistant super alloys are considered very important in the aerospace industry, mainly for the application of engine components. Approximately 50% of “hot section” gas turbine components are manufactured from nickel-based super alloys, as reported in [1][2]. Nickel-based super alloys are also logical choices in other key industrial sectors such as oil and gas industry components [3] and nuclear power plant components [4]. The main reason for using nickel-based super alloys is their exceptional material characteristics, such as mechanical strength, resistance to surface degradation and creep resistance at elevated temperatures. Many types of nickel-based super alloys have been developed over the years [5]. One commonly used nickel-based super alloy is Inconel 625. Because it contains niobium and molybdenum in a nickel chromium matrix, this super alloy is able to maintain its mechanical properties and corrosion resistance at temperatures up to 650°C [6]. These excellent properties are retainable even without precipitation heat treatment. Components made from Inconel 625 are widely used in the aerospace industry in the “hot section” of gas turbine engines and in nuclear reactors, the chemical industry and other high temperature and corrosion applications [7][8][9][10].

The most common manufacturing method for final products is machining. In general, nickel-based alloys are considered to be difficult-to-cut materials, mainly due to their low thermal conductivity, high hardness and low elastic modulus [1]. This results in a high thermo-mechanical load of the component and the cutting tool. Subsequently, progressive tool wear is observed in machining of nickel-based alloys [11][12]. In response, new part manufacturing approaches are being explored with the aim of minimizing material

removal through the cutting process, which can save both input material and tool costs. Considering current industrial and economical demands, additive manufacturing (AM) of Inconel 625 complex shaped components is one reasonable option [13][14].

Wire arc additive manufacturing (WAAM) is a subtype of AM that combines wire as a feedstock and electric arc as a heat source [16][17]. WAAM excels over other metal AM technologies in particular owing to its high deposition rates and low equipment costs [18]. On the other hand, it cannot fully match the geometrical complexity and precision of powder bed AM methods (e.g. Selective Laser Melting or Laser Metal Deposition) [15]. Hence, WAAM is suitable especially for manufacturing or repairing larger components which would typically be machined after an additive process [19][20][21].

WAAM techniques can be further categorized by the type of arc welding process. According to current studies, [19][21][22] three basic techniques are being examined and used for research and development of prototypes. These welding techniques are gas tungsten arc welding (GTAW) [23][24][25], gas metal arc welding (GMAW) [26][27][28] and plasma arc welding (PAW) [22][29]. The advantage of the GMAW process lies in the fact that an electrode is a consumable wire which is standardly coaxial with the welding torch. In contrast, GTAW has the consumable wire added non-coaxially, rendering it more difficult for 5-axis control. While PAW can achieve very high productivity, the heat input is also quite high [30]. It is not beneficial for smaller, more precise parts. Moreover, the PAW process lead and tilt angles of the welding torch could be harmful for the manufacturing result. Thus, the PAW process is not suitable for 5-axis WAAM technology. For the purposes of WAAM, GMAW modification, known as Cold Metal Transfer (CMT), is suitable [31][32].

CMT is a modified GMAW process based on short-circuiting transfer, where movement of the wire feedstock at high frequencies (up to 80 Hz) combined with the welding current and voltage control improves the properties of the welding process. The key improvements are elimination of spatter and considerably lower heat input [33]. As an alternative to a standard continuous welding strategy, a CMT welding unit is also capable of a spot welding strategy. The spot welding strategy has lower productivity and higher consumption of shielding gas. However, it excels in terms of very low heat input and very precise material cladding in comparison with a standard continuous welding strategy. Fine details can be manufactured even on thin walled components or in sections with problematic heat dissipation [34].

In relation to the current state of the art, numerous papers focus on WAAM manufacturing of Inconel alloys. Most papers address Inconel 718 (IN718) alloy, and only [26][28][37][41][42][43] focus on Inconel 625. WAAM components from Inconel 718 require post-process heat treatment [9], which is no obstacle for manufacturing blank parts. According to [9][35], Inconel 625 (IN625) does not require post-process heat treatment. This property makes IN625 more suitable for hybrid WAAM [36] of a finished component in one machine. Analysis of material properties is a common step in the process of developing a technology strategy. Analysis enables an understanding of the elementary principles of the manufacturing process. To develop a reliable manufacturing method, it is necessary to study the material properties of samples manufactured using various complementary operations and methods.

Summarizing the current state of the art of Wire Arc Additive Manufacturing of Inconel, information from research papers can be sorted into these categories:

(i) *Shielding gas influence*

In [37], the influence of 4 different shielding gases for WAAM of IN625 was studied. The gas mixture of 97.5% Ar and 2.5% CO2 performed better than the other gas mixtures in terms of YS, UTS and hardness. However, other studies [38][39] mentioned the importance of having a helium proportion of about 20–25%. A proper solution could be to use a gas mixture [40] designed for nickel based super alloys from a specialized gas company (Messer Group GmbH).

(ii) *Welding strategy*

Study [41] focused on comparison of the material properties of a standard CMT welding process and a pulse CMT welding process during the WAAM of IN625. Both techniques demonstrated YS and UTS results that were about 20% better than a casted sample. The CMT pulse manufactured sample was even slightly better (5–15%) than the standard CMT in YS, UTS and hardness. There are similarities between CMT pulse welding and CMT spot welding. Investigation of the material properties of a IN625 WAAM CMT spot welding strategy can further confirm or contradict the results from [41].

(iii) *Inter layer technological operations*

Various other technological factors affecting WAAM of IN718 have been examined in published papers. These are interpass cleaning of the weld surface [44] and interpass rolling of the weld seams with 50 kN and 75 kN [23]. In both cases, the results show that the positive influence of these treatments is not quite clear. Interpass rolling increased hardness but other mechanical properties were worse than without interpass rolling. Effects of interpass cleaning have not been observed.

(iv) *Material analysis*

Standard analytical tools in contemporary research include optical microstructure and macrostructure analysis, hardness analysis and SEM analysis. Many studies also rely on tensile strength testing and EDS analysis. To keep the present research relevant to the current state of the art, all of these standard types of analyses were performed. It is clear that the properties of Inconel 625 alloy, which should retain its tensile strength at elevated temperatures, make a tensile strength test at 650°C [6] very relevant for this research.

The main goal of this paper is to expand the state of the art in WAAM of Inconel 625. A GMAW CMT spot welding strategy will be tested and compared with a standard GMAW CMT continuous welding strategy. Complex material analyses will be performed, including: metallography, SEM (Scanning Electron Microscope), x-ray tomography, hardness, wear resistance and tensile strength. The last two material properties will be investigated at room temperature (20°C) and also at an elevated temperature of 650°C.

2 Materials, Experimental Setup And Methods

2.1 Materials and shielding gas

To implement the experiment, it was necessary to define and obtain welding and substrate material along with shielding gas. The essential materials used in the experiments are specified in the tables below (Table 1, Table 2 and Table 3).

Thermanit welding wire Ø 1 mm from Voestalpine Böhler Welding GmbH was used as an input material. The chemical composition and elementary mechanical properties of the wire are shown in Table 1.

Steel plates were selected as a substrate material. It was found [39] that welding Inconel 625 on weldable carbon steel is suitable. Plates made of EN - S235 JRG 1 were prepared for the following dimensions: steel plate 110 x 110 x 12 mm. The chemical composition and elementary mechanical properties of the plates are depicted in Table 2.

The shielding gas is a mixture designed by Messer Group GmbH for welding nickel-based alloys. The composition of the shielding gas mixture is provided in Table 3. The gas flow is controlled by the flow valve to a level of 13 or 15 l/min depending on the welding strategy. Although [37] presents testing of different gasses, the experiments implemented for the present paper rely on recommendations by Messer welding experts with industrial experience. The presence of helium in the mixture also aligns with research papers [38][39].

Table 1
Composition and properties of Thermanit 625 filler wire material

Chemical composition [wt %]												
C	Si	Mn	P	S	Cr	Mo	Ni	Cu	Ti	Al	Nb	Fe
< 0.1	< 0.1	< 0.1	0.003	0.001	22.3	8.8	64.6	< 0.1	0.2	0.2	3.5	0.2
Mechanical properties												
T [°C]		Rp 0.2 [MPa]			Rm [MPa]		A [%]			KV [J]		
20		≥ 460			≥ 740		≥ 30			≥ 60		

Table 2
nposition and properties of the substrate material EN - S235 JRG 1

emical composition [wt %]					
	Mn	P	S	Cu	N
7	< 1.4	< 0.035	< 0.035	< 0.55	< 0.012
chanical properties					
C]	Rp 0.2 [MPa]	Rm [MPa]	A [%]	KV [J]	
	≥ 235	≥ 375	≥ 26	≥ 21	

Table 3
Composition of the shielding gas

Chemical composition [wt %]			
CO2	H2	He	Ar
0.12	2.0	30.0	67.88

2.2 Experimental setup, strategy and samples

An innovative patented hybrid manufacturing method using WAAM was used for the metal deposition process. This method utilizes a welding unit as a part of a 3-axis vertical CNC milling centre. The welding torch is in the same workspace as the milling spindle. The hybrid manufacturing method is characterized by this sequence of operations [36]: (i) deposition of a metal layer using electric arc welding in a protective atmosphere, (ii) machining aimed at creating a geometrically defined surface for another weld deposit, (iii) mechanical surface cleaning, and (iv) air cooling/cleaning. At the cost of slightly reduced productivity, WAAM on a defined machined surface greatly increases the manufactured part's precision and possible shape complexity. Inter-operational cleaning also reduces porosity and the probability of internal material defects [36]. The method was also used in a study for welding stainless steel [45].

The experiments were performed on a 3-axis CNC hybrid machine. A Bridgeport VMC 500 XP vertical machining center with a Heidenhain iTNC 530 control system was combined with a CMT Advanced 4000R welding unit. A Robacta Drive CMT W pro welding torch was positioned parallel to the milling spindle. Other accessories required for hybrid WAAM technology (wire feeder, air cleaning/cooling, water cooled table) were incorporated into the machine setup.

The experimental samples were manufactured using the welding parameters presented in Table 4. The layers were manufactured one after another in the manner shown in Fig. 3, where weld cladding starts and directions are described. The size of the shape is approximately 110 x 110 mm with a height of 50 mm from the 12 mm-thick substrate. For both of the welding strategies described in Table 4, two identical

samples were manufactured, resulting in a total of four samples. The welding parameters were optimized during the preceding research through visual inspection only. The material properties were unknown and therefore, performing material tests is an overall advancement in WAAM technology research at the CTU.

The specimens for the material tests were extracted from samples using an EDM (Electrical Discharge Machining) process. The layout of all specimens is shown in Fig. 5 and Fig. 6. There are two types of tensile specimens: (i) Horizontal and (ii) Vertical.

Table 4
Welding parameters

Continuous welding strategy – A samples		**Spot welding strategy – B samples**	
wire feed [m/min]	7.1	wire feed [m/min]	8.1
torch travel speed [m/min]	0.5	CMT parameter (droplets) [-]	-2.5
current [A]	100	pitch distance of spots [mm]	3.0
voltage [V]	14.8	current [A]	186
shielding gas flow [l/min]	15	voltage [V]	14.6
		shielding gas flow [l/min]	13

Table 5
Auxiliary technological data

layer height (continuous)	**1.2 mm**	**layer height (spot)**	**1.7 mm**
milling tool	Walter F4041 B22.050.Z04	milling inserts	Iscar H490 ANKX 120508PNTR
cutting speed	50 m/min	feed per tooth	0.2 mm/tooth

2.3 Analytical methods

To analyse the material properties of the manufactured samples, the material tests shown in Table 6 were performed. These tests are divided into structural tests and mechanical tests:

Table 6
List of material tests

Structural
Metallography
SEM (Scanning Electron Microscope)
X-ray tomography
Mechanical
Hardness (Vickers)
Wear resistance (20°C and 650°C) – Pin-on-disc
Tensile strength (20°C and 650°C)

(i) Metallography (specimens 33A, 33B, 34A, 34B)

The microstructure of the specimens was revealed by electrolytic etching in an electrolyte consisting of a 10% aqueous solution of oxalic acid with a Struers Polipower DC source with the following setup: 2.5V, 20 s. The microstructure was then observed using a Carl Zeiss Jena Neophot 32 light optical microscope.

(ii) SEM (specimens 35A, 35B)

A Jeol JSM-7600F SEM microscope equipped with an EDS detector and EBSD detector was used to make observations. The acceleration voltage was 15 KV. Images were taken with a LEI detector (secondary electrons) and LABE detector (back scattered electrons). The secondary electrons provide information about the structure and morphology of the observed sample. The back scattered electrons slightly reflect the chemical composition of the observed sample.

(iii) X-ray tomography (specimens 31A, 31B, 32A, 32B)

X-ray tomography was conducted using a Zeiss Metrotom 1500 system with a 225kV and 2K detector with a pixel size of 0.2 mm. Samples with a square cross-section of 3 x 3 mm were selected to obtain high resolution images of the scanned point cloud. The CT system settings for the tested samples were acceleration voltage of 225kV, with a current of 460 µA, integration time of 600 ms with activated image averaging from 3 pictures in each angular position for noise reduction and a 2 mm cooper filter to adjust the X-ray spectrum to eliminate beam hardening artefacts to obtain the best imaging. Magnification of 8.8x led to a final voxel size of 0.0227 mm. The porosity analysis was evaluated using VG Max software with an Easypore algorithm; all pores bigger than 8 voxels were considered in the statistics, which is a common rule to exclude image noise from the evaluation. Each sample scan contained more than 700 million voxels.

(iv) Hardness (specimens 29A, 29B)

The Vickers hardness (load 10 kg, HV10) of the specimens was measured using a Struers Duramin 40-AC3 universal hardness testing machine.

(v) Wear resistance (specimens 27A, 27B)

Dry sliding tribological tests were carried out on the specimens (ground with water-cooled 800 grit SiC paper) at 20°C and 650°C using an Anton Paar THT-S-CE 0000 pin-on-disc tribometer. The static friction partner was an Al_2O_3 ball with a diameter of 6 mm. The test parameters were: wear track radius 3 mm, normal force 5 N and linear speed of the revolving partner 5 cm/s with a stop condition of 5000 laps. The relative humidity in the laboratory was 37%. The results of the pin-on-disc testing (i.e., profiles of wear track on both the ball and the revolving friction partner) were evaluated using an Olympus DSX1000 light optical microscope.

(vi) Tensile strength (specimens 1-20A, 1-20B)

An Instron 3369 machine was used for the measurements. The crosshead speed was 2.4 mm/min. All the tests were performed according to the EN ISO 6892-1:2009 standard. Five measured specimens were used for each set.

3 Results And Discussion

3.1 Metallography

Micrographs of the etched 33A, 33B, 34A and 34B specimens obtained by LOM showed the presence of the layers characteristic for the additive manufacturing technologies as well as molten pool boundaries (MPBs). The microstructure is coarser closer to the boundaries of these layers, where it can act as a crack nucleation site. The observed areas are significant with the dendritic structure in the same direction. However, the microstructure is not cellular as in the case of 3D printing technologies, but is more reminiscent of the welded/cladded microstructure. This can be seen in Fig. 7.

The boundaries of the dendrites are rich with dark particles (Fig. 8); depending on the chemical composition of the filler wire, these may be Nb, Mo, or Ti rich carbides. Further investigation was conducted using SEM.

In the spot welded strategy samples (B), there are areas with polyhedric grains, which implies partial recrystallization (see Fig. 8). This leads to the conclusion that, in the B set-up, the energy input was insufficient for partial recrystallization. The structure of the spot welded samples (B) is more inhomogeneous but also more fine-grained than the structure of the continuous welding samples (A). A more finegrained structure could indicate better mechanical properties. These mechanical properties will be further investigated.

There was no observable structural difference between specimens 33A and 34A or between specimens 33B and 34B. Thus, no structural difference was observed along the layer building direction for either of the welding strategies.

3.2 Scanning electron microscopy (SEM)

Scanning electron microscopy did not show any notable differences between welding strategies A and B or any notable differences along the layer building direction. The scanning electron microscopy observations were mainly focused on documenting the particles located at the recrystallized grain boundaries and dendrite boundaries. The chemical composition analysis of the particles was performed via EDXS analysis.

The two micrograms shown below (Fig. 9 and Fig. 10) document the microstructure of partially recrystallized grains and dendritic structure in specimen 33B. These two microstructural states are regularly repeated with respect of the clad 3D printed layers and their thermal influence on each other.

The micrograms below document the morphology and chemical composition of the cladded layers (Fig. 11). Oriented dendritic grains, which grow from partially recrystallized grains with particles at their grain boundaries, are visible. This type of microstructure corresponds with layer cladding and heat involving the previous layer.

Chemical composition map measurements (Fig. 12) confirmed the homogeneity of the 3D printed samples, with segregation of niobium and precipitation of niobium rich phases. The chemical maps at lower magnification are listed below.

Chemical composition measurements were taken at the same measurement spot. Spectrum 4 represents the global chemical composition and spectrum 2 and 3 correspond with the niobium base particles. The results of the EDXS measurements are shown in Fig. 13.

The global chemical composition corresponds with the filler metal used for 3D printing. The measured chemical composition in spectrum 2 and 3 confirms the higher niobium content, but the particles are small. The surrounding base material was involved in the measurements and affected the results.

EDXS measurements of the chemical composition for the precipitated particles were taken using higher magnification. The chemical composition maps are summarized in Fig. 14 below.

The measurement of the chemical composition of the niobium part is shown in Fig. 15. The chemical composition led to the result that the particle is niobium carbide with a niobium content of over 24 weight percent.

3.3 X-ray tomography

The basic statistics and visualizations generated for all samples and results from the porosity analysis are summed up in Fig. 16.

Figure 16 indicates that there is a significant difference between the pore count and size on samples made by continuous and those made by spot welding. The largest pore detected among all of the samples was recorded on sample 31B (horizontal sample made by spot welding), which had a volume of 7.3×10^{-3} mm³, which is 619 voxels in total (Fig. 16). The smallest pore size and the only pore detected in the entirety of specimen 32A had a pore volume of 9.0×10^{-5} mm³ in a total of 8 voxels. This is the smallest pore size that may be practically detected by the given CT system and parameter settings for the specific material and sample size.

Porosity was evaluated as a defect volume ratio; in other words, the ratio between total material volume and total defect volume, both calculated in mm^3. The porosity analysis results are described in Table 7.

Table 7
Porosity analysis results

Sample	Material volume [mm3]	Defect volume [mm3]	Defect volume ratio [%]	Total pores detected
31A	270.15213	0.00099	0.00036	9
31B	268.44717	0.01568	0.00584	19
32A	270.15582	0.00009	0.00003	1
32B	270.49005	0.00544	0.00201	33

Both of the continuous welding samples had significantly lower porosity than the spot welding samples. The largest pore detected on a continuous welded sample was detected on sample 31A with a volume of 1.3×10^{-4} mm³ and 11 voxels. The largest and the only pore detected on sample 32A was a pore with a volume of 9.0×10^{-5} mm³ in a total of 8 voxels. The largest pore detected from all of the samples was recorded on sample 31B (horizontal sample made by spot welding) with a volume of 7.3×10^{-3} mm³ which is 619 voxels in total. The largest pore detected on vertical sample 32B made by spot welding had a volume of 4.7×10^{-4} mm³ with 40 voxels in total.

3.4 Hardness

The hardness measurement was carried out on specimens 29A and 29B. The measurement layout along with the results are presented by the graph in Fig. 17. The average hardness of specimen 29A is 252 ± 14 HV10, and the average hardness of specimen 29B is 251 ± 13 HV10. Based on these results, there is no hardness variance between sets A and B. The scatter of the hardness values along the x-axis corresponds with the heterogeneous microstructure after the manufacturing process.

3.5 Wear resistance

The results of the pin-on-disc test were evaluated as the volume loss in cubic millimetres for both the pin and the disc. The wear profile of the pin and disc was measured using optical microscopy profiling in the Z-axis and then calculated by approximative equations given in the standard ASTM G99-5 [47]. The

profile of the wear tracks and loss area were then calculated as the volume loss (see Fig. 18). The dynamic coefficient of friction was recorded during the test. The significant difference between the 20°C and 650°C tests can be seen (Fig. 19) in the dynamic friction coefficient and also in the volume loss of the disc. The ball wear was approximately the same in all four cases, while the volume loss at 20°C and 650°C on the side of the disc is two to three times higher than by the static friction partner.

The dry sliding dynamic friction coefficient (see records in Fig. 19) in the room temperature test fluctuated around an average of 0.75. Significant peaks up to 0.9 can be seen in the middle of the total time. This may be caused by an uneven microstructure with the particles causing a plowing effect. In the case of the elevated temperature test at 650°C, the friction coefficient was stable at 0.15–0.2.

This can lead to the conclusion that this alloy performs better at higher temperatures. Nevertheless, the wear track and wear mechanisms are different (oxidation and adhesion at elevated temperature) and must be considered in future product design. The cross-section of the wear track and its 3D profiles can be seen in Fig. 20. The wear track after the high temperature test was shallow with a stacked volume in the middle.

3.6 Tensile strength

The results of tensile tests at a temperature of 20°C are shown in Table 8 and Fig. 22. The standard deviations of YS and UTS are small, which corresponds to the excellent homogenous structure of the samples. The standard deviation of elongation values is quite noticeable, which is probably caused by the different position of rupture on the specimen during the tensile test.

For both the continuous welding and spot welding strategies, the UTS in the horizontal direction is slightly higher than in the vertical direction (2% continuous, 8% spot). This phenomenon does not apply for YS. Overall, the spot welding strategy specimen has a YS that is 13% higher in the horizontal direction and 1% lower in the vertical direction than the continuous welding strategy specimen. Similarly, the UTS of the spot welding strategy specimen is 20% higher in the horizontal direction and 13% higher in the vertical direction than of the continuous welding strategy specimen.

Table 9 and Fig. 23 show the results of tensile tests of WAAM samples of Inconel 625 at a temperature of 650°C. Deviations for YS and UTS are similarly small, which corresponds to the excellent homogenous structure of the samples. Deviations for elongation values are also quite noticeable and are caused by the different position of rupture on the specimen during the tensile test.

Even at 650°C, the WAAM Inconel 625 retains most of its mechanical properties. However, in comparison with an annealed bar of Inconel 625 [6], the decrease of YS and UTS is more significant. While annealed Inconel 625 at 650°C has approximately 15% YS and lower UTS compared to its 20°C values, the spot welded specimens show a decrease of approx. 26% and the continuous welded specimens shows a decrease of approx. 30% compared to the 20°C values. The comparison is described in Table 10 and Table 11.

The last comparison pertains to the published tensile strength results of WAAM Inconel 625 – see Table 12. Both the continuous and spot welded specimens have the highest YS of the published results. The UTS of the spot welded specimen is also the highest among the published results, while the UTS of the continuous welded specimen is slightly below the average.

Table 8
Mechanical properties of Inconel 625 welds at 20°C

	YS [MPa]	UTS [MPa]	Elongation [%]
continuous welding – horizontal	369 ± 16	643 ± 16	55.0 ± 2.3
continuous welding – vertical	392 ± 10	630 ± 31	49.6 ± 8.2
spot welding – horizontal	417 ± 4	773 ± 10	50.4 ± 8.5
spot welding – vertical	389 ± 8	715 ± 13	59.2 ± 2.0

Table 9
Mechanical properties of Inconel 625 welds at 650°C

	YS [MPa]	UTS [MPa]	Elongation [%]
continuous welding – horizontal	271 ± 24	450 ± 22	45.8 ± 6.5
continuous welding – vertical	276 ± 10	432 ± 20	58.0 ± 9.1
spot welding – horizontal	301 ± 11	581 ± 17	46.7 ± 3.5
spot welding – vertical	282 ± 12	534 ± 19	51.0 ± 2.2

Table 10
Mechanical properties of Inconel 625 welds: comparison at 20°C and 650°C (vertical direction)

	20°C		650°C			
	YS [MPa]	UTS [MPa]	YS [MPa]	UTS [MPa]	YS decrease [-]	UTS decrease [-]
annealed [6]	492	965	419	812	15%	16%
continuous welding	392 ± 10	630 ± 31	276 ± 10	432 ± 20	30%	31%
spot welding	389 ± 8	715 ± 13	282 ± 12	534 ± 19	28%	25%

Table 11
Mechanical properties of Inconel 625 welds: comparison at 20°C and 650°C (horizontal direction)

	20°C		650°C			
	YS [MPa]	UTS [MPa]	YS [MPa]	UTS [MPa]	YS decrease [-]	UTS decrease [-]
annealed [6]	492	965	419	812	15%	16%
continuous welding	369 ± 16	643 ± 16	271 ± 24	450 ± 22	27%	30%
spot welding	417 ± 8	773 ± 13	301 ± 11	581 ± 17	28%	25%

Table 12
Comparison of published results at 20°C (vertical direction)

	YS difference [-]	UTS difference [-]	Elongation difference [-]
continuous welding strategy	reference	reference	reference
spot welding strategy	-1%	+ 13%	+ 19%
torch speed 0.48 m/min [26]	-4%	+ 3%	-6%
torch speed 0.54 m/min [26]	0%	+ 7%	-10%
torch speed 0.60 m/min [26]	+ 2%	+ 9%	-13%
weave torch trajectory [28]	-	+ 2%	+ 21%
multiple clads [28]	-	+ 8%	+ 19%
shielding gas 2.5% CO_2 [37]	+ 11%	+ 19%	-
sh. gas 3% He, 1.5% H_2 [37]	-10%	+ 11%	-
shielding gas 5% H_2 [37]	-20%	+ 11%	-
shielding gas 99.999% Ar [37]	-14%	+ 11%	-
as deposited [43]	-5%	+ 4%	+ 13%
30 min heat-threated [43]	-7%	+ 6%	-3%
1-hour heat-threated [43]	-8%	+ 7%	-13%
2 hours heat-threated [43]	+ 1%	+ 9%	-7%
short arc welding [41]	-35%	-8%	+ 31%
pulsed arc welding [41]	-28%	-6%	+ 33%

4 Conclusions

The aim of this study was to analyse the material properties of an innovative GMAW CMT spot welding strategy used for Inconel 625 material. The GMAW CMT spot welding strategy is suitable for building complex shapes, fine details and thin walled components, mainly due to the lower heat input. The results of this innovative welding strategy were compared to the standard GMAW CMT continuous welding strategy performed by the authors of the study and also to published results pertaining to WAAM of Inconel 625. The material analysis demonstrated that the GMAW CMT spot welding strategy has the following benefits and differences.

(1) Metallography showed that the structure of the samples is quite similar to the welded/cladded structure. This was expected given the character of WAAM technology. The spot welded strategy samples were affected by partial grain recrystallization and their structure is more fine-grained. Thus, the microstructure of the spot welded strategy samples is more inhomogeneous than the continuous welded strategy samples.

(2) SEM was used to analyse the details of the microstructure. No element composition difference was observed between the continuous (A) and spot (B) welding strategies. The element composition corresponds to the Thermanit 625 filler wire that was used. The presence of precipitated niobium particles was confirmed. These particles were quite small (2–5μm). The chemical composition led to the result that the particle is niobium carbide with a niobium content of over 24 weight percent.
(3) X-ray tomography proved that there were no significant internal defects in the manufactured structure of either the continuous welding strategy or the spot welding strategy samples. It is reasonable to say that the pores detected on the continuous welding samples were fewer in total and much smaller in size than the pores on the spot welded samples. On the other hand, all defect volume ratios are on a very small scale compared to the total volume of material. Even the largest porosity of 0.00584% is a very good result compared to, for example, PBF-LB technology, where the lowest porosity detected with the same technology was in the range of 0.02%, where other researchers achieve the lowest levels of porosity in the range of 0. 8% with PBF using metallography analysis [48].
(4) Based on the hardness measurement results, there is no hardness variance between the continuous strategy and spot strategy welded samples. The scatter of the hardness values along the layer building direction corresponds with the heterogeneous microstructure after the manufacturing process.
(5) Wear resistance measurements lead to the conclusion that this alloy performs better at higher temperatures. Nevertheless, the wear track and wear mechanisms are different (oxidation and adhesion at elevated temperature) and must be considered in future product design. The spot welding strategy samples performed even better at an elevated temperature of 650°C, as the volume of its wear was about half of that of the continuous strategy welded samples.
(6) Tensile strength test results clearly show that the tensile mechanical properties of the spot welded specimens are better than those of the continuous welded specimens. The YS is similar for both strategies, but the UTS of the spot welded specimens is approx. 15% higher at 20°C, and the retention of

the mechanical properties (YS and UTS) at a temperature of 650°C is approx. 4% better. The spot welding strategy achieved the second highest UTS amongst the published results of Inconel 625 welds.

Declarations

Acknowledgments The authors would like to express their thanks for the support provided by ESIF, EU Operational Programme Research, Development and Education.

Availability of data and material The authors confirm that the data and material supporting the findings of this work are available within the article.

Author contribution Not applicable.

Funding Supported from the EU Operational Programme Research, Development and Education, and from the Center of Advanced Aerospace Technology (CZ.02.1.01/0.0/0.0/16_019/0000826), Faculty of Mechanical Engineering, Czech Technical University in Prague.

Ethics approval The article follows the guidelines of the Committee on Publication Ethics (COPE) and involves no studies on human or animal subjects.

Consent to participate Not applicable. The article involves no studies on humans.

Consent for publication Not applicable. The article involves no studies on humans.

Competing interests The authors declare no competing interests.

References

1. E.O Ezugwu, J. Bonney, Y. Yamane, An overview of the machinability of aeroengine alloys, Journal of Materials Processing Technology, Volume 134, Issue 2, 2003, Pages 233-253, ISSN 0924-0136, https://doi.org/10.1016/S0924-0136(02)01042-7.
2. Gopala Rao Thellaputta, Pulcharu Subhash Chandra, C.S.P. Rao, Machinability of Nickel Based Superalloys: A Review, Materials Today: Proceedings, Volume 4, Issue 2, Part A, 2017, Pages 3712-3721, ISSN 2214-7853, https://doi.org/10.1016/j.matpr.2017.02.266.
3. Sankara Papavinasam, Chapter 3 - Materials, Editor(s): Sankara Papavinasam, Corrosion Control in the Oil and Gas Industry, Gulf Professional Publishing, 2014, Pages 133-177, ISBN 9780123970220, https://doi.org/10.1016/B978-0-12-397022-0.00003-0.
4. F. King, 4 - General corrosion in nuclear reactor components and nuclear waste disposal systems, Editor(s): Damien Féron, In Woodhead Publishing Series in Energy, Nuclear Corrosion Science and Engineering, Woodhead Publishing, 2012, Pages 77-103, ISBN 9781845697655, https://doi.org/10.1533/9780857095343.2.77.

5. I.A Choudhury, M.A El-Baradie, Machinability of nickel-base super alloys: a general review, Journal of Materials Processing Technology, Volume 77, Issues 1–3, 1998, Pages 278-284, ISSN 0924-0136, https://doi.org/10.1016/S0924-0136(97)00429-9.
6. Special Metals Corporation Products, INCONEL® alloy 625, www.specialmetals.com/products
7. Shankar V., Rao KBS, Mannan S., (2001) Microstructure and mechanical properties of Inconel 625 superalloy. J Nucl Mater 288(2-3):222–232
8. G.P. Dinda, A.K. Dasgupta, J. Mazumder, Laser aided direct metal deposition of Inconel 625 superalloy: microstructural evolution and thermal stability, Mater. Sci. Eng. A 509 (2009) 98–104.
9. K.D. Ramkumar, W.S. Abraham, V. Viyash, N. Arivazhagan, A.M. Rabel, Investigations on the microstructure, tensile strength and high temperature corrosion behaviour of Inconel 625 and Inconel 718 dissimilar joints, Journal of Manufacturing Processes. 25 (2017) 306–322.
10. Wang Yangfan, Chen Xizhang, Su Chuanchu, Microstructure and mechanical properties of Inconel 625 fabricated by wire-arc additive manufacturing, Surface and Coatings Technology, Volume 374, 2019, Pages 116-123,
11. Alagan, N.T., Hoier, P., Zeman, P. et al. Effects of high-pressure cooling in the flank and rake faces of WC tool on the tool wear mechanism and process conditions in turning of alloy 718. Wear 434-435 (2019) 102922.
12. Alagan, N.T., Zeman, P. et al. Investigation of micro-textured cutting tools used for face turning of alloy 718 with high-pressure cooling. Journal of Manufacturing Processes, 37 (2019), 606-616.
13. Asit Kumar Parida, Kalipada Maity, Comparison the machinability of Inconel 718, Inconel 625 and Monel 400 in hot turning operation, Engineering Science and Technology, an International Journal, Volume 21, Issue 3, 2018, Pages 364-370.
14. S. Li, Q. Wei, Y. Shi, Z. Zhu, D. Zhang, Microstructure characteristics of Inconel 625 superalloy manufactured by selective laser melting, J. Mater. Sci. Technol. 31 (2015) 946–952.
15. S.W. Williams, F. Martina, A.C. Addison, J. Ding, G. Pardal, and P. Colegrove, Mater. Sci. Technol. 32, 641 (2016).
16. R. Acheson: 'Automatic welding apparatus for weld build-up and method of achieving weld build-up'; US patent no. 4 952 769 1990.
17. Williams, S.W., Martina, F., Addison, A.C., Ding, J., Pardal, G., Colegrove, P.: Wire + arc additive manufacturing. Mater. Sci. Technol. 32(7), 641–647 (2016). https://doi.org/10.1179/1743284715Y.0000000073
18. https://www.3dmpwire.com/project-details/goals-and-objectives/
19. D. Ding, Z. Pan, D. Cuiuri, H. Li, Wire-feed additive manufacturing of metal components: technologies, developments and future interests, Int. J. Adv. Manuf. Technol. 81 (2015) 465-481.
20. Busachi, Alessandro & Erkoyuncu, John & Colegrove, Paul & Martina, Filomeno & Ding, Jialuo. (2015). Designing a WAAM Based Manufacturing System for Defence Applications. Procedia CIRP. 37. 48-53. 10.1016/j.procir.2015.08.085.

21. Rodrigues, Tiago & Duarte, Valdemar & Miranda, R.M. & Santos, Telmo & Oliveira, J. P.. (2019). Current Status and Perspectives on Wire and Arc Additive Manufacturing (WAAM). Materials. 12. 1121. 10.3390/ma12071121.
22. Y. Wang, X. Chen, S.V. Konovalov, Additive manufacturing based on welding arc: a low-cost method, J. Surf. Invest-x-ray+ 11 (2017) 1317–1328.
23. Xiangfang Xu, Supriyo Ganguly, Jialuo Ding, Cui Er Seow, Stewart Williams, Enhancing mechanical properties of wire+arc additively manufactured INCONEL 718 superalloy through in-process thermomechanical processing, Materials & Design, Volume 160, 2018, Pages 1042-1051, ISSN 0264-1275, https://doi.org/10.1016/j.matdes.2018.10.038.
24. L.N. Zhang, O.A. Ojo, Corrosion behavior of wire arc additive manufactured Inconel 718 superalloy, Journal of Alloys and Compounds, Volume 829, 2020, 154455, ISSN 0925-8388, https://doi.org/10.1016/j.jallcom.2020.154455.
25. Asala, Gbenga & Khan, Abdul & Andersson, Joel & Ojo, O.A. (2017). Microstructural Analyses of ATI 718Plus Produced by Wire-ARC Additive Manufacturing Process. Metallurgical and Materials Transactions A. 48. 1-18. 10.1007/s11661-017-4162-2.
26. Wang Yangfan, Chen Xizhang, Su Chuanchu, Microstructure and mechanical properties of Inconel 625 fabricated by wire-arc additive manufacturing, Surface and Coatings Technology, Volume 374, 2019, Pages 116-123, ISSN 0257-8972, https://doi.org/10.1016/j.surfcoat.2019.05.079.
27. Jan Hönnige, Cui Er Seow, Supriyo Ganguly, Xiangfang Xu, Sandra Cabeza, Harry Coules, Stewart Williams, Study of residual stress and microstructural evolution in as-deposited and inter-pass rolled wire plus arc additively manufactured Inconel 718 alloy after ageing treatment, Materials Science and Engineering: A, Volume 801, 2021, 140368, ISSN 0921-5093, https://doi.org/10.1016/j.msea.2020.140368.
28. Jiang, Qi & Zhang, Peilei & Zhishui, Yu & Shi, Haichuan & Li, Shaowei & Wu, Di & Yan, Hua & Ye, Xin & Chen, Jieshi. (2020). Microstructure and Mechanical Properties of Thick-Walled INCONEL 625 Alloy Manufactured by WAAM with Different Torch Paths. Advanced Engineering Materials. 23. 10.1002/adem.202000728.
29. Bhujangrao, Trunal & Veiga, Fernando & Suarez, Alfredo & Iriondo, Edurne & Mata, Franck. (2020). High-Temperature Mechanical Properties of IN718 Alloy: Comparison of Additive Manufactured and Wrought Samples. Crystals. 10. 689. 10.3390/cryst10080689.
30. Artaza, Teresa & Bhujangrao, Trunal & Suarez, Alfredo & Veiga, Fernando & Lamikiz, Aitzol. (2020). Influence of Heat Input on the Formation of Laves Phases and Hot Cracking in Plasma Arc Welding (PAW) Additive Manufacturing of Inconel 718. Metals. 10. 771. 10.3390/met10060771.
31. Kah, Paul & Suoranta, Raimo & Martikainen, J.. (2013). Advanced gas metal arc welding processes. The International Journal of Advanced Manufacturing Technology. 67. 655-674. 10.1007/s00170-012-4513-5.
32. Tapiola, Jaakko. (2017). Cold Metal Transfer cladding of wear and corrosion resistant coatings in engine applications. 10.13140/RG.2.2.15573.52963.

33. Selvi S., Vishvaksenan A., & Rajasekar E. (2018) Coldmetal transfer (CMT) technology - an overview. In Defence Technology (Vol. 14, issue 1, pp. 28–44). Elsevier ltd. https://doi.org/10.1016/j.dt.2017.08.002
34. https://www.fronius.com/en/welding-technology/info-centre/magazine/2019/cmt-cycle-step
35. J.D. Whittenberger (1992) A Review of: “SUPERALLOYS II” edited by CT. Sims, N.S. Stoloff, and W.C. Hagel, A Wiley-Interscience Publication John Wiley & Sons, New York, NY 615 pages, hardcover, 1987, Materials and Manufacturing Processes, 7:3, 463-468, DOI: 10.1080/10426919208947432
36. https://patents.google.com/patent/CZ306654B6/cs
37. Jurić, Ivan & Garasic, Ivica & Bušić, Matija & Kožuh, Zoran. (2018). Influence of Shielding Gas Composition on Structure and Mechanical Properties of Wire and Arc Additive Manufactured Inconel 625. JOM. 71. 10.1007/s11837-018-3151-2.
38. Baixo, Carlos & Dutra, Jair. (2011). Effect of Shielding Gas and Transfer Mode on the Application of 625 Alloy in Carbon Steel. Welding International. 25. 903-909. 10.1080/09507116.2010.527480.
39. Elango, P. & Sethuraman, Balaguru. (2015). Welding Parameters for Inconel 625 Overlay on Carbon Steel using GMAW. Indian Journal of Science and Technology. 8. 10.17485/ijst/2015/v8i1/84309.
40. https://elmemesser.lv/en/products/gas-in-cylinders/welding-and-cutting-gases/
41. Mookara, Rama & Seman, Saravanan & Ren, Jayaganthan & Amirthalingam, Murugaiyan. (2021). Influence of droplet transfer behaviour on the microstructure, mechanical properties and corrosion resistance of wire arc additively manufactured Inconel (IN) 625 components. Welding in the World. 65. 10.1007/s40194-020-01043-6.
42. Cheepu, Murali Mohan & Lee, Chang & Cho, Sang-Myung. (2020). Microstructural Characteristics of Wire Arc Additive Manufacturing with Inconel 625 by Super-TIG Welding. Transactions of the Indian Institute of Metals. 73. 10.1007/s12666-020-01915-x.
43. Tanvir, Ali Newaz Mohammad & Ahsan, Md. Rumman & Ji, Changwook & Hawkins, Wayne & Bates, Brian & Kim, Duck Bong. (2019). Heat treatment effects on Inconel 625 components fabricated by wire + arc additive manufacturing (WAAM)—part 1: microstructural characterization. International Journal of Advanced Manufacturing Technology. 1-14. 10.1007/s00170-019-03828-6.
44. Xiangfang Xu, Jialuo Ding, Supriyo Ganguly, Stewart Williams, Investigation of process factors affecting mechanical properties of INCONEL 718 superalloy in wire + arc additive manufacture process, Journal of Materials Processing Technology, Volume 265, 2019, Pages 201-209, ISSN 0924-0136, https://doi.org/10.1016/j.jmatprotec.2018.10.023.
45. Mašek, Petr & Fornusek, T. & Zeman, Pavel & Bucko, Michal & Smolik, J. & Heinrich, P.. (2019). MACHINABILITY THE AISI 316 STAINLESS STEEL AFTER PROCESSING BY VARIOUS METHODS OF 3D PRINTING. MM Science Journal. 2019. 3338-3346. 10.17973/MMSJ.2019_11_2019091.
46. https://www.specialmetals.com/documents/technical-bulletins/inconel/inconel-alloy-625.pdf
47. ASTM G99-05 Standard Test Method for Wear Testing with a Pin-on-Disk Apparatus

48. AlFaify, A., Hughes, J. and Ridgway, K. (2019), "Controlling the porosity of 316L stainless steel parts manufactured via the powder bed fusion process", Rapid Prototyping Journal, Vol. 25 No. 1, pp. 162-175. https://doi.org/10.1108/RPJ-11-2017-0226

Figures

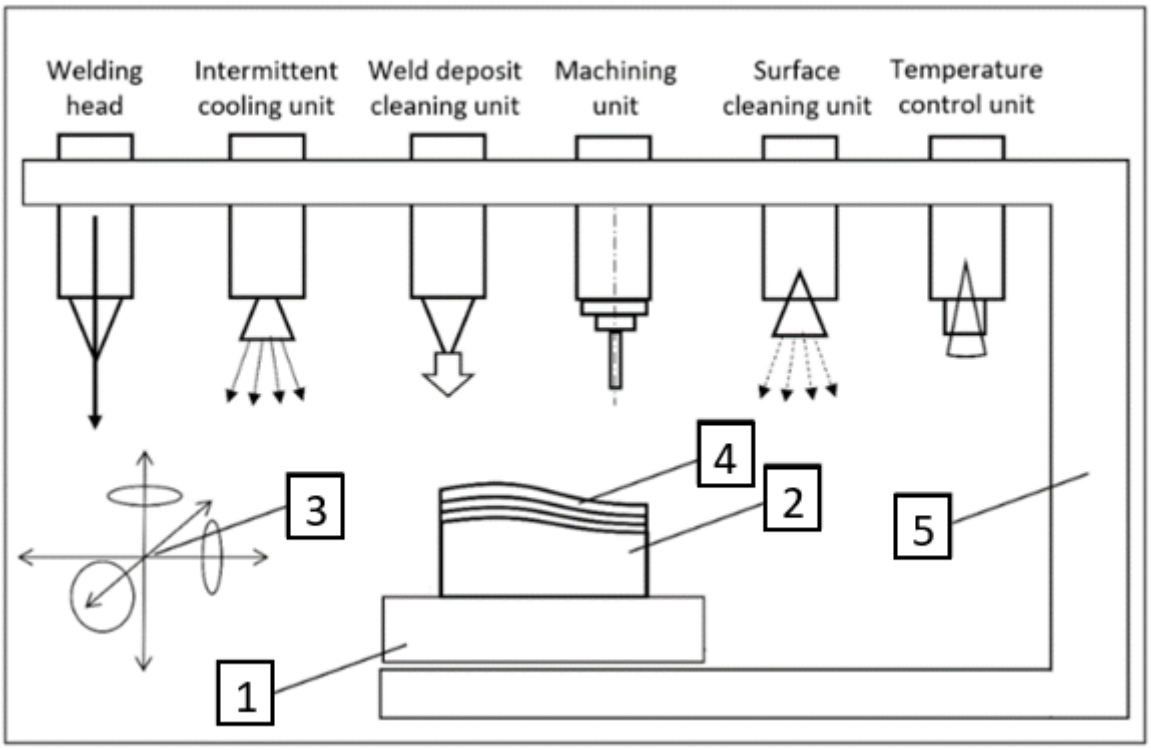

Figure 1

WAAM method for building parts. 1 - machine tool table with inner cooling; 2 - basic material; 3 - machine tool coordinate system; 4 - welded material; 5 - frame of the machine tool

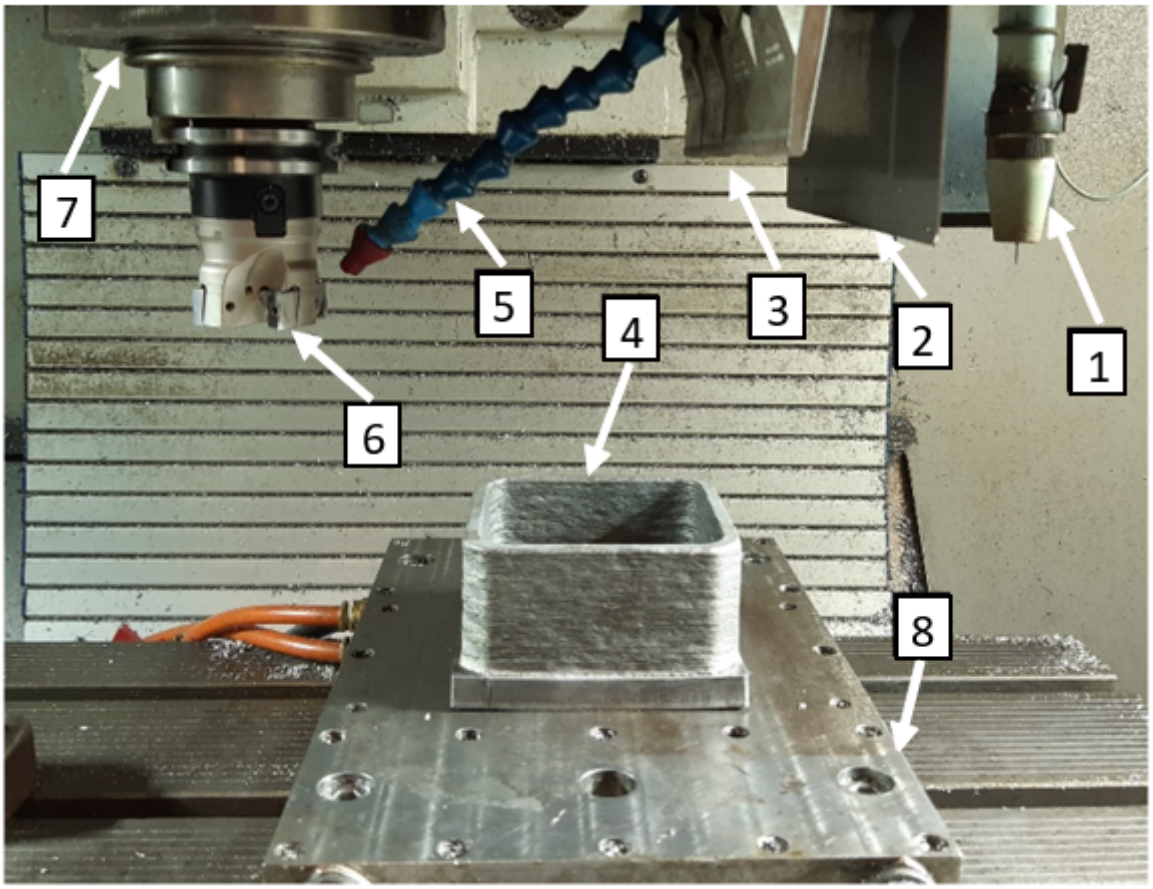

Figure 2

Experimental machine workspace. 1 – welding torch; 2 – welding process shielding; 3 – air blade pressure cleaning; 4 – manufactured part; 5 – milling process cooling; 6 – milling tool; 7 – spindle; 8 – worktable with inner cooling

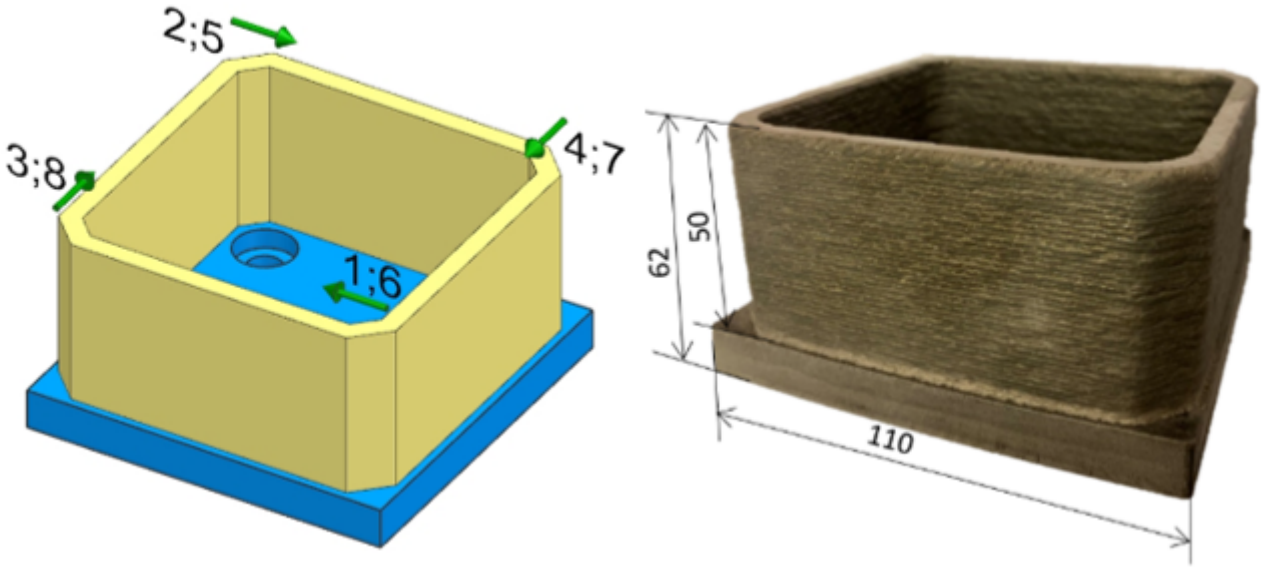

Figure 3

Scheme of chronological order of weld cladding starts and directions (left), dimensions of manufactured samples (right)

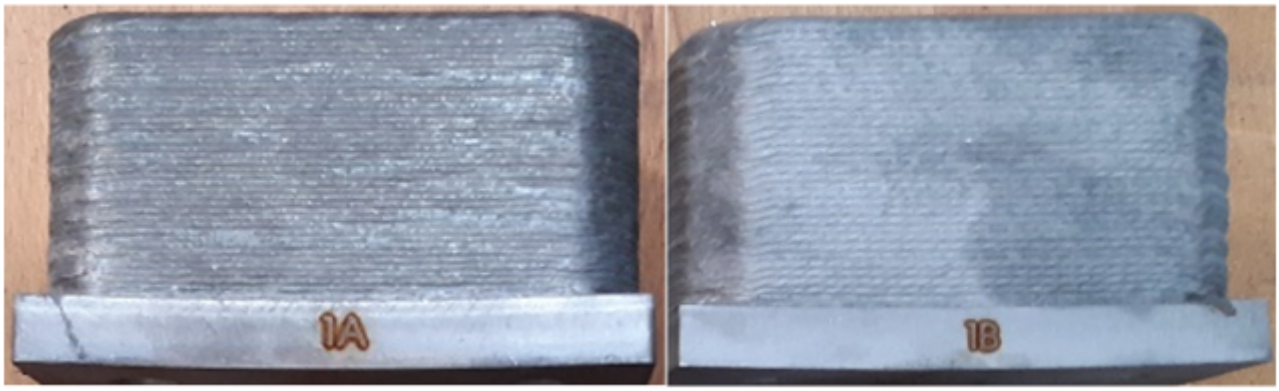

Figure 4

Detail of manufactured samples: type A wall structure – continuous welding (left), type B wall structure – spot welding (right)

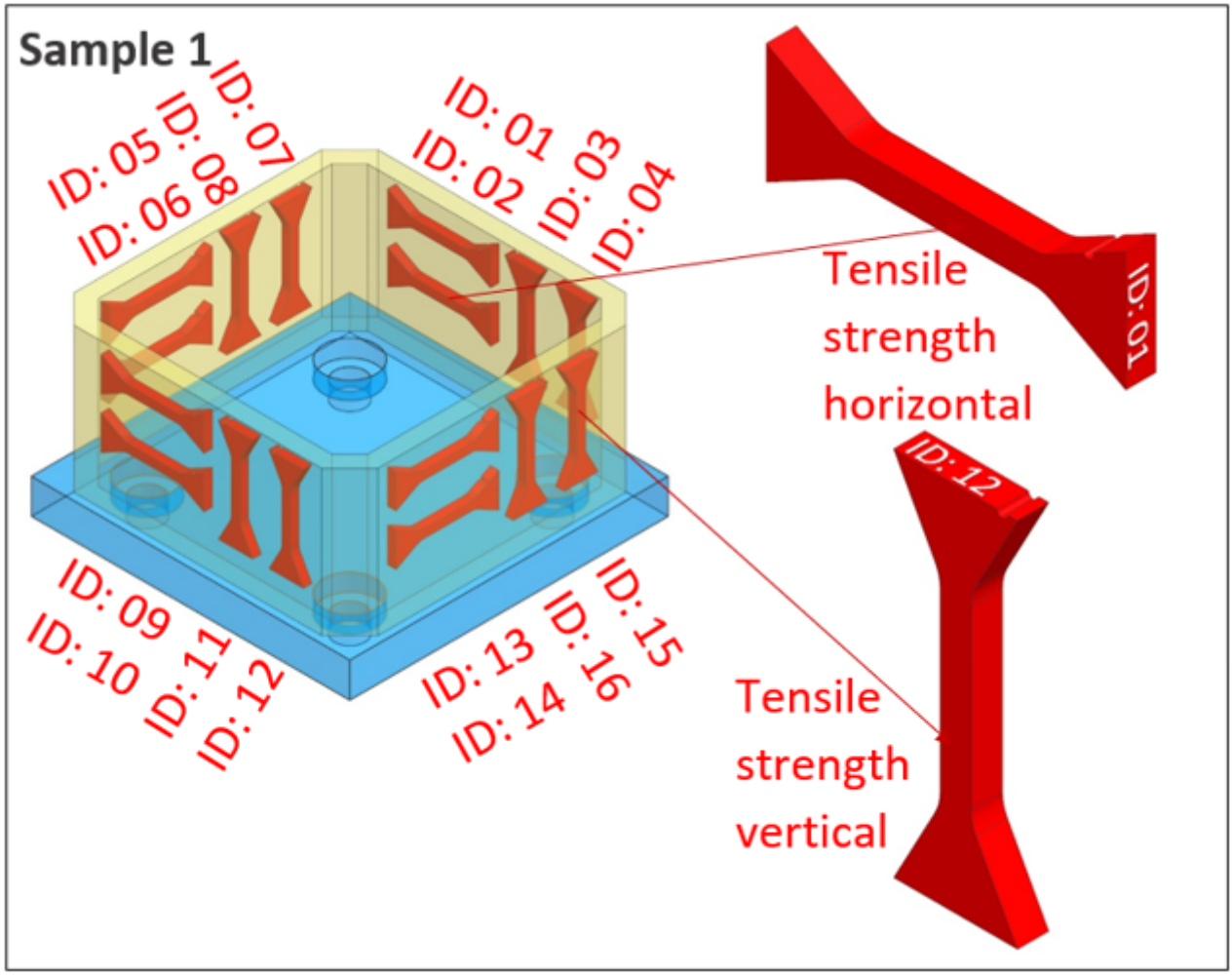

Figure 5

Specimen layout in sample 1

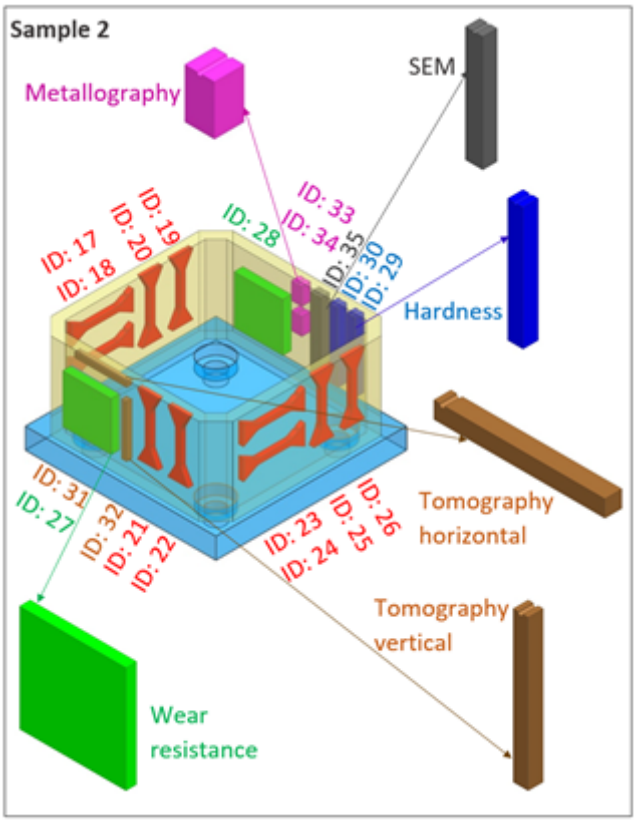

Figure 6

Specimen layout in sample 2

Figure 7

Macrostructure comparison of A - continuous welding strategy (left) and B - spot welding strategy (right) specimens

Figure 8

Detailed structural comparison of A - continuous welding strategy (left) and B – spot welding strategy (right) specimens

Figure 9

Detail of the partially recrystallized grains (33B)

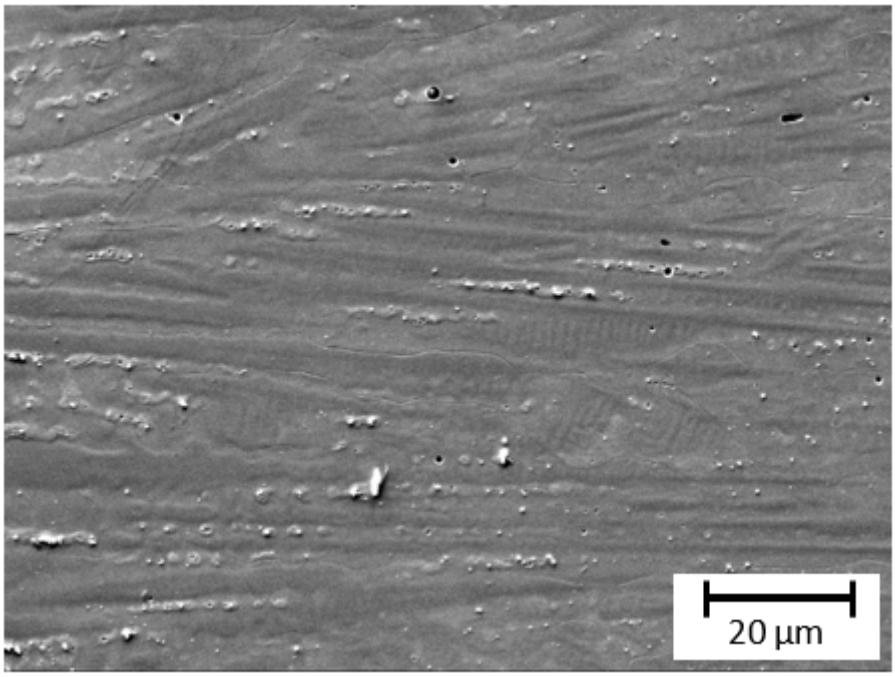

Figure 10

Detail of the dendritic structure (33B)

Figure 11

Comparison of secondary and back scattered electron images (33B)

Figure 12

Chemical composition maps (33B)

Figure 13

EDXS measurement (33B)

Figure 14

Chemical maps of precipitated particles (33B)

Figure 15

Detailed EDXS measurement (33B)

Figure 16

Porosity analysis on samples – histogram of defect sizes and frequencies

Figure 17

HV10 hardness along samples 29A and 29B

Figure 18

Volume loss of the static and revolving friction partners after the pin-on-disc test

Figure 19

Dynamic friction coefficient during the pin-on-disc test at 21 and 650 °C

Figure 20

Profiles of specimen wear tracks

Figure 21

Tensile testing – example photography of ruptured specimen (spot welding – vertical - 20°C)

Figure 22

Mechanical properties of Inconel 625 welds at 20°C

Figure 23

Mechanical properties of Inconel 625 welds at 650°C